TAO, Vol. 11, No. 3, 591-608, September 2000

Rupture Process of the 1999 Chi-Chi, Taiwan, Earthquake from the Inversion of Teleseismic Data

Shiann-Jong Lee[1, *] and Kuo-Fong Ma[1]

(Manuscript received 4 July 1999, in final form 20 February 2000)

ABSTRACT

We investigated 22 broadband teleseismic records of the 1999 Chi-Chi earthquake to determine its temporal and spatial slip distribution. The results show an anomalous large slip region centered about 40 to 50 km north of the hypocenter at a shallow depth. The largest amount of slip was about 6 ~ 10 m. The slip near the vicinity of the hypocenter had a relatively smaller amount of slip. The spatial slip distribution pattern coincides well with the observed strong-motion displacement and surface break. In the largest dislocation region, the slip was dominated by dip-slip. Some strike-slip component in the middle of the fault was found during the rupture. The Southern portion of the fault showed relatively constant rupture velocity with an average slip of about 1 m, whereas the northern portion of the fault showed significant variations in rupture velocity and produced a large amount of slip.

(Key words: Teleseismic, Inversion, Rupture Process)

1. INTRODUCTION

The 21 September 1999 (01:47:12) Chi-Chi earthquake (M_L=7.3) was one of the most destructive earthquakes in Taiwan during the past 100 years. Faulting during the earthquake was interpreted as reverse, left-lateral faulting on a low-angle plane along the Chelungpu fault (Lee et. al, 2000), characterized by a long rupture length (over 80 km) and long duration of about 30 s (Ma et al. 1999). Field observations showed the surface breaks varied along the fault rupture. The largest displacement on surface was nearly 9.8 m, measured at 45 km north of the hypocenter. This complicated surface break possibly indicates the complexity of the rupture process of the earthquake.

Slip distribution determinations of large earthquakes are important in that they provide insight into the spatial and temporal details of the earthquake rupture process. The analysis of source models provides an understanding of the consistencies and variations in rupture kine-

[1]Institute of Geophysics, National Central University, Taiwan, ROC

[*]*Corresponding author address*: Mr. Shiann-Jong Lee, Institute of Geophysics, National Central University, Chung-Li, 320 Taiwan, ROC; E-mail: lcc@rupture.gep.ncu.edu.tw

matics and dynamics from event to event. In addition to that, finite-fault source studies can also furnish information beneficial to a wide range of seismological investigations and earthquake engineering applications. For such a large event as the 1999 Chi-Chi, Taiwan, earthquake, the understanding of its rupture process is crucial for further studies.

The 1999 Chi-Chi earthquake was well recorded by the dense strong motion network (Liu et al. 1999). However, due to the possibility of complex fault geometry and structure, the inversion of strong motion waveforms dose not readily lead to a quick determination of fault slip distribution. However, this large earthquake was also well recorded by teleseismic stations worldwide, which provided a good opportunity to quickly determinate fault rupture behavior. These teleseismic data have good data quality and azimuthal coverage of the earthquake while providing first-order information on the complexity of the source of the earthquake.

2. DATA AND METHOD

The teleseismic stations chosen for this study are listed in Table 1. The stations were chosen for their epicentral distances between 40° to 100° to avoid the complexities of the earth's structure. The distribution of stations and waveforms are shown in Fig. 1. These data are digital recordings obtained from The Incorporated Research Institutions for Seismology (IRIS), and the stations we chose provide good coverage of azimuth from source. Instrument responses were deconvolved from the original recordings. We executed integral on each recording to obtain ground displacement without filtering. The record lengths used were 70 s, and the sampling rate used in inversion was 0.2 s.

For a large earthquake, the rupture fault plane can usually be represented as slip distribution on a planar surface. Here, we divided the fault plane into numerous subfaults, with each subfault having one point source (Fig. 2). The slip over the subfault area was contributed by the point source. The teleseismic synthetic Green's function was generated by the generalized ray method (Langston and Helmberger 1975). The displacement recorded at a given station could then be represented as the linear sum of slip contributed from these subfaults. The rupture on each subfault had an appropriate delay in time, which depended on the rupture velocity we assumed. The delay time between the neighboring subfaults could be estimated as the ratio of the size of the subfault to the rupture velocity. The velocity model used to compute the teleseismic Green's functions was a three-layer over a half-space as shown in Table 2, which is the average crust model of the global earth (Takeo and Kanamori 1992). The synthetic Green's functions in this study included more important conversions between phases occurring at the free surface as well as the more important internal conversions. The source time function was given as a triangle with a 1-s rise and a 1-s fall, for a total source time duration of 2.0 s. We also further considered multiple-time window analysis on each subfault to accommodate any the possible complexity of the slip function on each subfault, allowing for spatial variations in rise time.

The observed and synthetic waveforms could, thus, be formed as a system of linear equations:

$$Ax=b, \quad (1)$$

where A is the matrix of Green's functions, b is the data vector, and x is the solution matrix of the subfault dislocation (slip). This system of liner equation is shown in Fig. 3. Each column of A is composed of the Green's functions, strung end to end, for a particular subfault and a particular mechanism (either strike-slip or dip-slip) for all the stations in the inversion. Similarly, b was formed by stringing all observation records end to end. Hence, each time point on each record was explicitly included in the inversion. The number of columns of A depended

Table 1. Station Parameters.

Station	Longitude	Latitude	Delta (°)	Azimuth	Back Azimuth	P Delay (sec)
ADK	-176.68	51.88	54.6	42.29	264.30	1.0
AFI	-171.78	-13.91	75.5	112.25	299.25	0.0
BORG	-21.32	64.75	87.1	344.75	34.160	2.2
CMB	-120.38	38.04	95.7	43.96	306.41	1.4
COLA	-147.85	64.879	69.2	27.12	281.89	1.6
COR	-120.30	44.59	90.1	39.92	304.70	1.2
CTAO	146.26	-20.09	50.0	148.28	329.19	0.0
DUG	-112.81	40.20	99.0	38.55	311.88	1.2
ESK	-3.21	55.32	88.1	331.76	49.28	2.4
FFC	-101.98	54.73	93.5	23.20	321.57	1.8
KBS	11.94	78.93	70.4	348.81	66.92	2.2
KDAK	-152.58	57.78	68.3	35.06	280.63	1.4
KIEV	29.21	50.69	73.1	318.38	73.11	2.4
KIP	-158.02	21.42	73.7	73.27	289.78	0.8
KONO	9.60	59.65	79.9	331.30	60.03	2.4
NEW	-117.12	48.26	91.4	34.42	309.24	1.6
PAB	-4.35	39.55	99.0	320.34	49.06	2.0
PAS	-118.17	34.15	99.5	46.00	307.44	1.2
PMG	147.15	-9.41	44.4	139.01	322.52	0.0
RAYN	45.50	23.520	68.4	287.00	72.54	2.0
SFJ	-50.62	67.00	89.3	356.65	7.82	2.2
TAU	147.32	-42.91	70.6	159.65	344.30	0.0

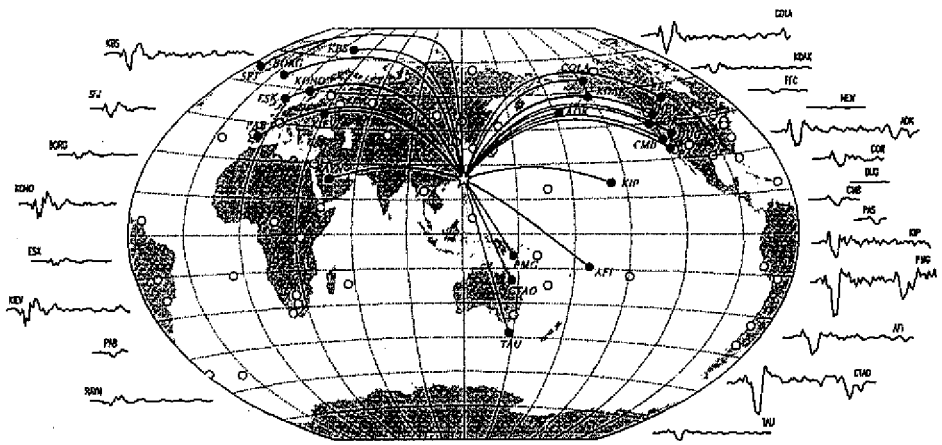

Fig. 1. Teleseismic station distribution and displacement waveforms. The solid circules indicate the stations used in the inversion. The open star indicates the epicenter.

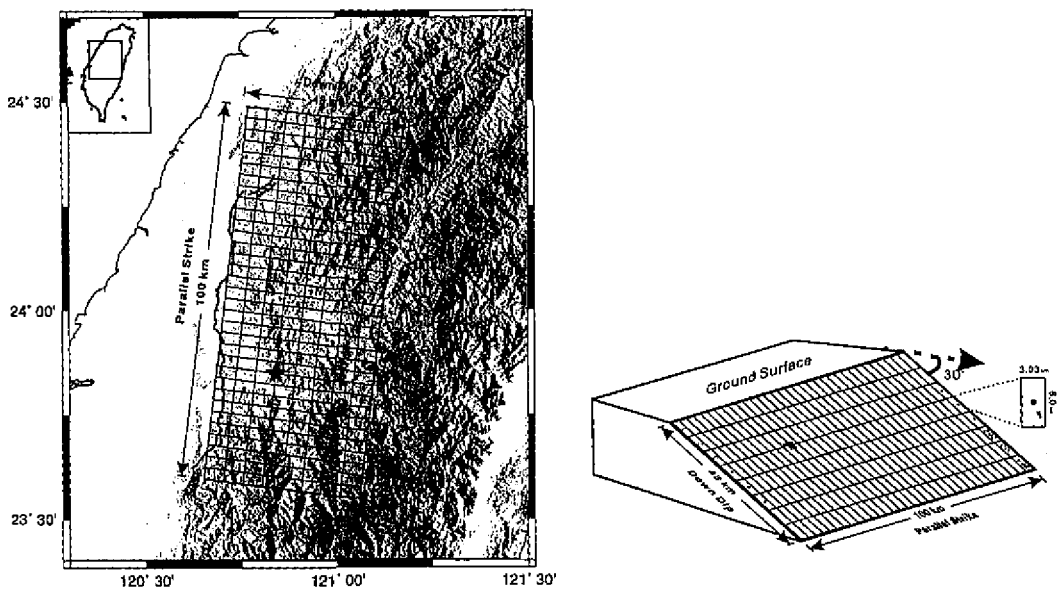

Fig. 2. Subfault layout of the fault model. The star indicates the hypocenter.

on the number of elements on x. Two cases were considered in this calculation. For a fixed focal mechanism, x contained the slip of each subfault with a specific slip vector as the rake angle. For free rake angle calculations, the elements of x were the amounts of strike-slip and dip-slip dislocations on each subfault. Accordingly, the Green's functions in matrix A were

Table 2. Global velocity model.

V_P (km/sec)	V_S (km/sec)	Density (g/cm^3)	Thickness (km)
5.60	2.90	2.50	6.1
6.00	3.40	2.60	12.9
6.80	4.00	3.00	30.0

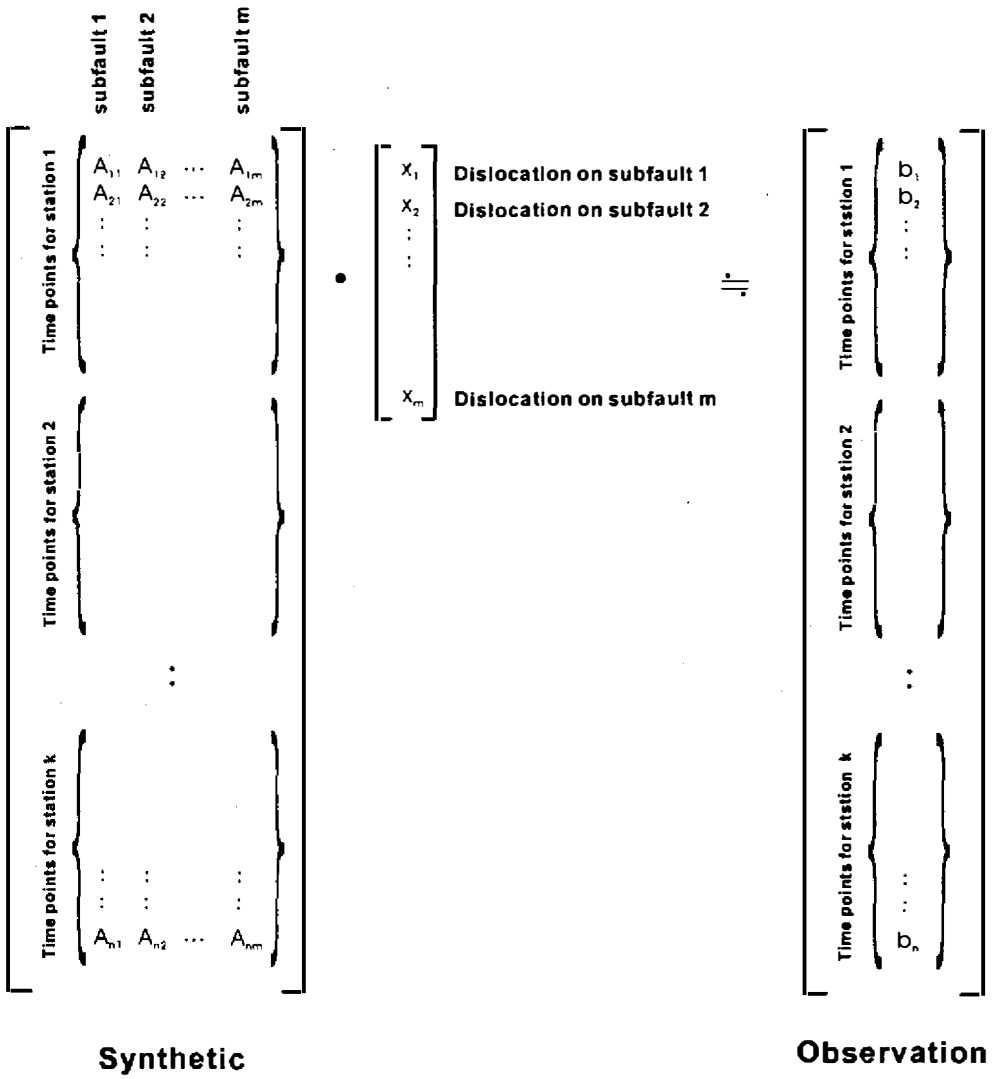

Fig. 3. Schemata of the least-squares waveform inversion [equation (1)].

also calculated for the strike-slip and dip-slip components, respectively, to construct the form as equation (1). We solved equation (1) using positive constraints of linear least squares. Other stability constraints have previously been discussed by Hartzell and Heaton (1983). This inversion method has successfully been used in analyzing the slip distribution and rupture processes of many large earthquakes, e.g., the 1983 Imperial Valley, California, earthquake (Hartzell and Heaton 1983), the 1992 Landers, California earthquake (Wald and Heaton 1994), and the 1994 Northridge, California earthquake (Wald and Heaton 1996).

Here we divided the fault area into 264 subfaults, with 33 subfaults along the strike and 8 down-dip, giving each subfault a length of 3.03 km and a down-dip width of 3 km (Fig. 2). This is a compromising method to represent variable slip along the fault. The subfault synthetic seismograms were convolved with a dislocation time history, which was represented by the time integral of an isosceles triangle with a duration of 2 s. The rupture velocity was assumed to be 2.5 km/s, which is about 80% of the shear-wave velocity. In the multiple-time window analysis, we allowed each subfault to slip in any one of six identical 2.0-s time windows following the passage of the rupture front. Each window had an overlap of 1 s. A schematic diagram depicting the use of time windows is presented in Fig. 4. In this example, six windows are shown, but the ability to model local variations in particle displacements and rupture delays (rupture velocity variations) is apparent; rupture can be locally delayed and can vary in duration. With multiple-time window analysis, we can study the more complex characteristics of a fault rupture, such as variable duration of local slip histories and potential variations in rupture velocity.

3. RESULTS

3.1 Slip Distribution

The focal mechanism of the USGS CMT solution of strike = 356°, dip = 29° and rake = 66° was first used for the Green's function calculations. However, the strike from the CMT solution was somewhat different from the strike of the observed surface break of the Chelungpu fault with strike of about 3°. To test this uncertainty in the strike, we considered both mechanisms in the calculations. The slip distributions from these two mechanisms is shown in Fig. 5(a) and (b), respectively, for strikes of 356° and 3°. The overall slip distributions in the two models are similar. The misfits, defined as , are about 0.41 and 0.38 for strikes of 356° and 3°, respectively.

They both show most of the slips were located at depths shallower than the depth of the hypocenter. A large asperity was found at 20~50 km to the north of the hypocenter along the strike. The slip was anomalous large averaging about 3 m. The slip near the hypocenter vicinity was relatively small. The largest slip was located at about 45 km to the north of the hypocenter at a down-dip depth of 6 km, with a maximum slip of about 8m. There was some slip distributed south of the hypocenter, suggesting some bilateral rupture behavior with respect to this earthquake. However, it had a significantly small amount of slip compared with the slip to the north of the hypocenter.

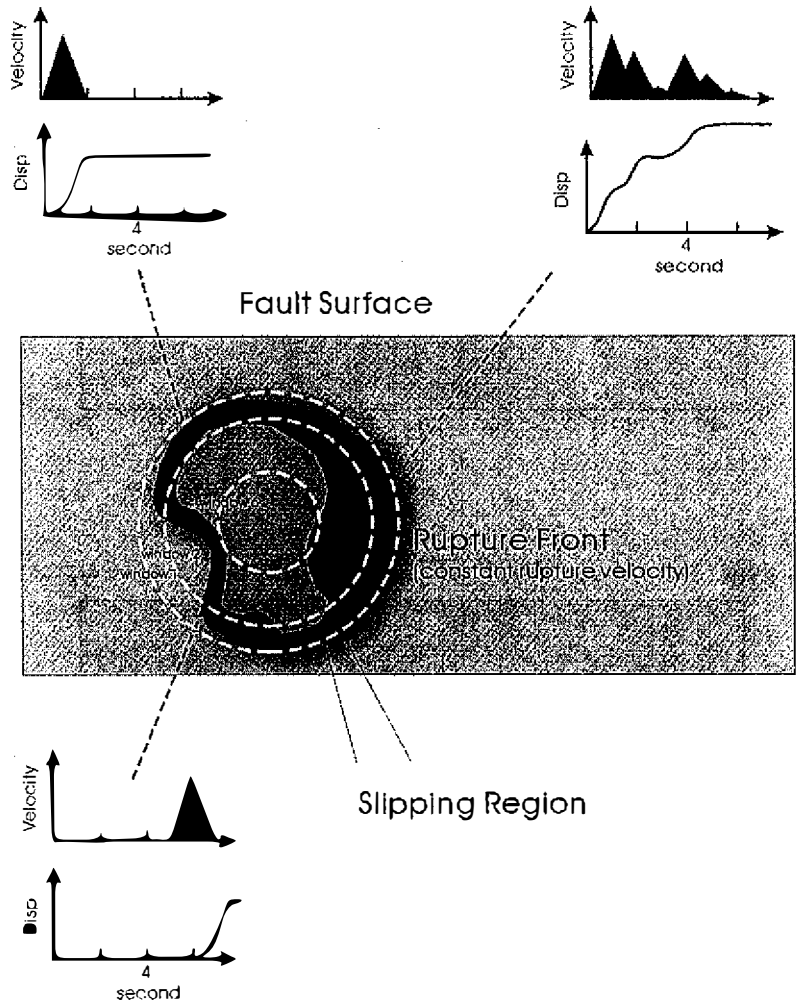

Fig. 4. Schematic diagram illustrating the use of multiple time windows.

The slip distribution also revealed some significant slip located at the deeper part of the fault plane. To examine the slips in deeper depths, we decreased the down-dip width in the fault dimension with the fault width of only 25 km. The result (Fig. 5(c)) shows similar slip distribution to that previously reported for the shallow portion. This indicates the reliability of the shallow slip distribution of this earthquake. However, the decrease in the fault plane reduced the amplitude of the waveforms with misfit of 0.39 and seismic moment. Although the slip at the shallower depth can explain most of the waveforms, the results still suggest that the slip at the deeper depth of the fault plane might have been real. Figure 6 compares the observed and synthetic waveforms for the fault geometry with length of 100 km and width of 45 km and strike of 3°, dip of 29° and rake of 66°. The waveforms are well explained for the first 40 s. After that some discrepancy is found between the observations and synthesized wave-

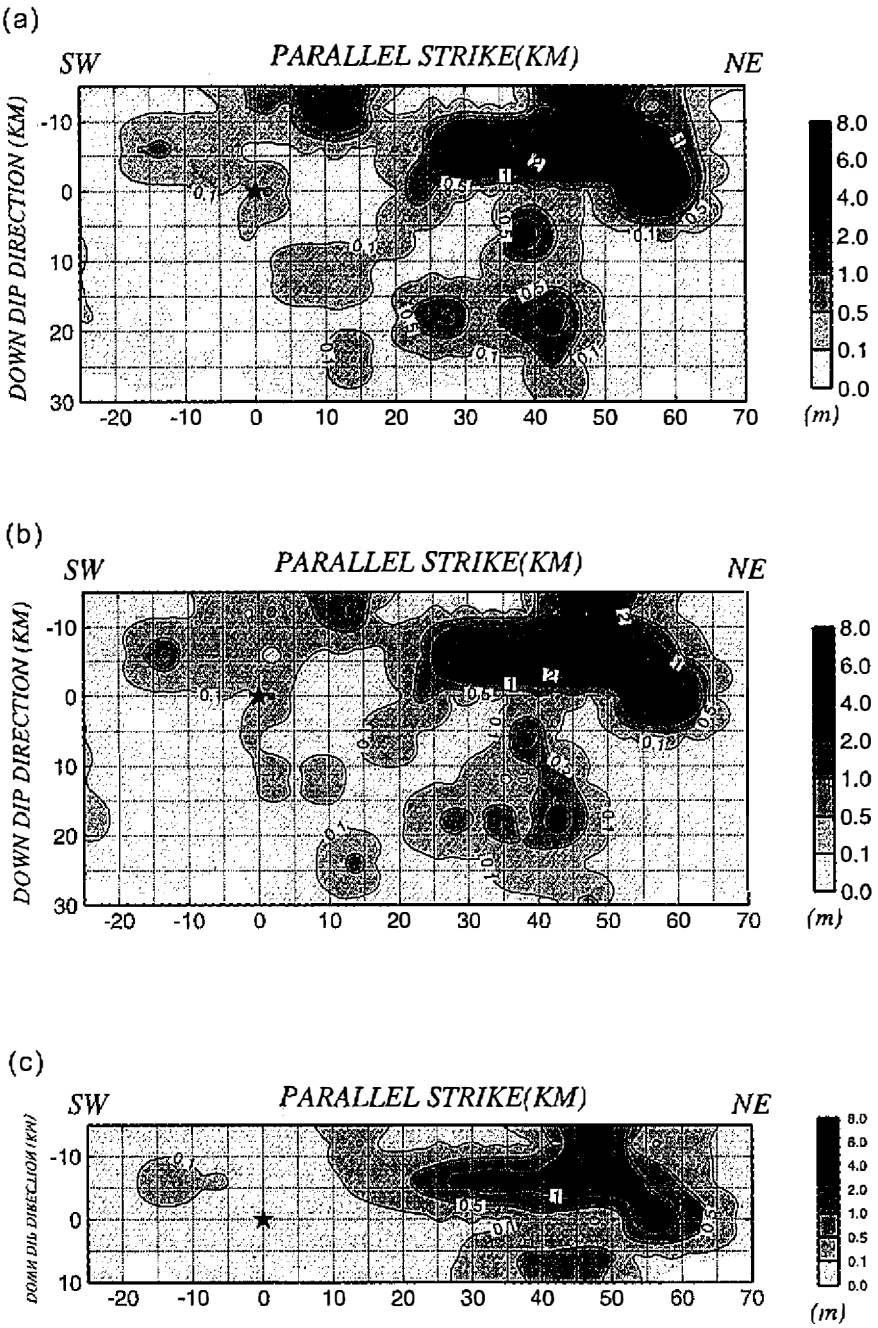

Fig. 5. Spatial slip distribution: (a) strike =356°, dip=29°, rake=66° (b) strike =3°, dip=29°, rake=66° and (c) shallow rupture model (half of the down-dip width) with strike =3°, dip=29°, rake=66°. The amount of slip is indicated by shading and contour as shown in the legend.

forms. This implies further modifications to the fault model or focal mechanisms might be necessary in the modeling.

3.2 Strike-Slip and Dip-Slip Distributions

Some field geological observations (e.g., Lee and Cheng 2000) showed variations in slip directions along the Chelungpu fault during the Chi-Chi earthquake. This implies that the slip angle might have varied during the faulting. To examine this possibility, we computed the

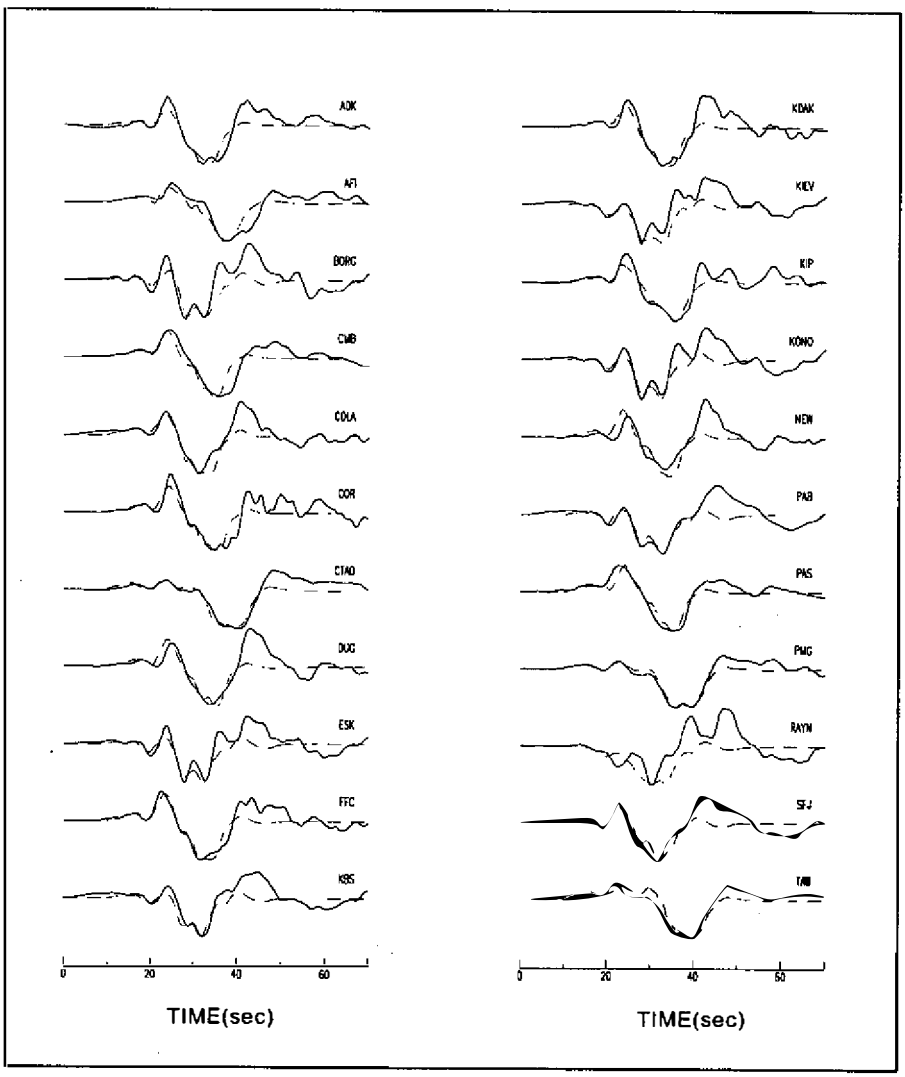

Fig. 6. Comparison of observations (solid lines) and synthetics (dashed lines) for the dislocation model of Figure 4 (a). All waveforms were normalized.

Green's functions for both the strike-slip and dip-slip mechanism to allow for the variations in rake angle from 0° to 90°. As mentioned in the previous section, by considering these two groups of the Green's functions in the inversion simultaneously, we were able to obtain the strike-slip and dip-slip components of slip on each subfault. The rake angle on each subfault was, therefore, determined from the vector sum of these two components, which allowed for the variations in rake angle during the rupture.

The slip distributions for the inversion of strike-slip and dip-slip are shown in Figs. 7 (a) and (b). The total slip distribution is shown in Fig. 7(c). In general, the overall slip distribution is similar to the one in the previous study. Also shown is a large asperity to the north of the hypocenter at shallow depth. The slip at deeper depth is also revealed. The largest amount of slip, located near the surface at about 45~50 km north from the hypocenter, is dominated by the dip-slip component. The slip vector has a complex variation during the rupture. Some strike-slip component is revealed during the rupture near the middle of the fault. The average rake angle in the fault plane was about 60°, which is similar to the rake angle determined by the CMT. The slip at the deeper depth had an average slip of about 1m. The synthetics of this calculation are shown in Fig. 8. The synthetics can now explain the overall observed waveforms well, and suggest the possibility of a variation in the rake angle during the rupture.

3.3 Temporal and Spatial Slip Distribution

We further considered multiple-time windows in this analysis. Six time windows were utilized at each subfault to enable us to make general observations about the time-history of the earthquake rupture. Considering the possible data resolution limitations on the teleseismic waveforms, for the temporal-spatial slip distribution analysis, we considered the focal mechanism as strike = 3°, dip = 29° and rake 66°. Even though this focal mechanism might not have been able to explain the observed waveforms at the later part well, previous studies have shown that this focal mechanism can represent the overall slip distribution pattern of the fault plane well. The final spatial-slip distribution of this multi-time windows model is shown in Fig. 9. Figure 10 shows the comparison of the observed and synthetic waveforms. Again, overall, the final spatial-slip distribution was similar to the patterns revealed in previous studies. This suggests that the spatial-slip distribution obtained in this study may be considered somewhat reliable.

Figure 11 shows the temporal-slip distribution of the fault plane for every second of the rupture. The propagation of the rupture front for the shallow slip region is also shown for every second. There is a significant variation in the rupture velocity. Near the hypocenter it is initially about 2.5 km/s, similar to common observations of about 85% of the shear wave velocity, but it decreases substantially to only about 1.2 km/s in the largest slip region. The initial rupture velocity was assumed to be a constant 2.5 km/s in the main part of the source region. We tried a range of values from 1.9 to 3.1 km/s but found 2.5 km/s to be the most suitable. After the execution of multiple-time window inversions, we found that the rupture velocities varied from 1.2 km/s to 4.0 km/s. The variations in the rupture velocity might have been associated with the stress or strength condition of the fault. The supersonic wave had also been examined in the 1979 Imperial Valley earthquake by Archuleta (1984) and in the 1992

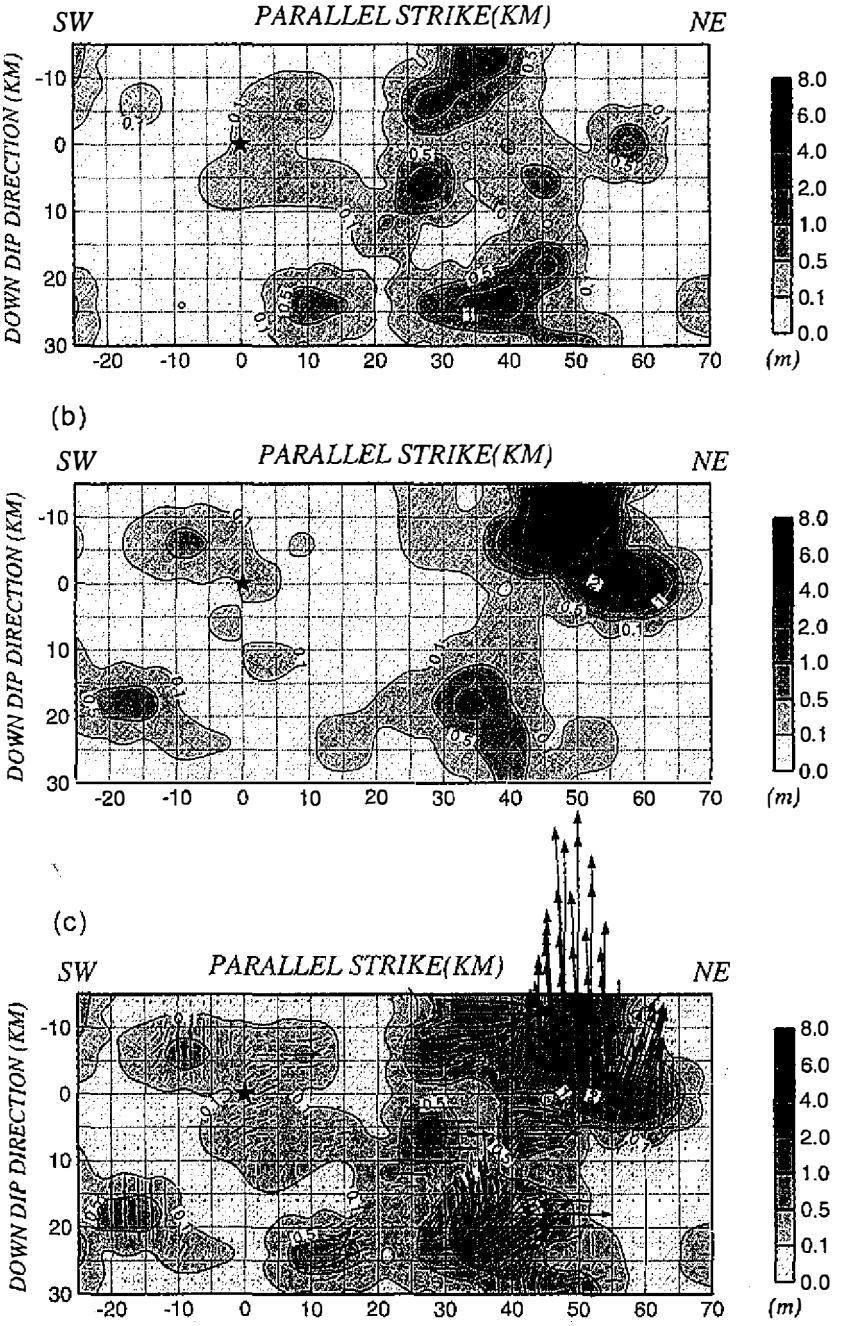

Fig. 7. (a) Strike-slip component, (b) dip-slip component, and (c) total slip distribution over the fault plane. The amount of slip is indicated by shading and contour as shown in the legend. The arrows indicate the slip vectors on the rupture plane.

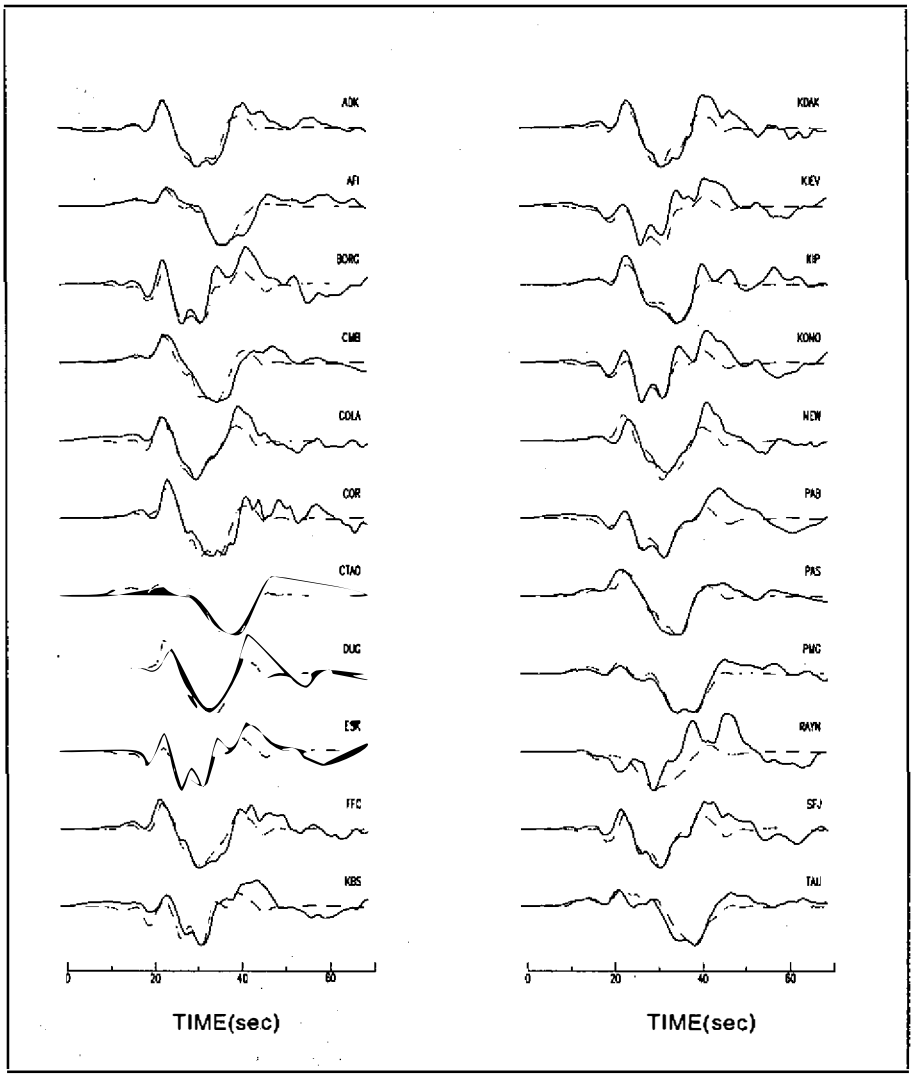

Fig. 8. Comparison of the observed (solid lines) and synthetic (dashed lines) waveforms for the decomposed model of Fig. 6.

Landers earthquake by Peyrat et al. (2000) and Wald and Heaton (1994). They concluded that the subsonic rupture velocities generally occurred within and near the low-stress areas on a fault, while supersonic ones dominated within highly-stressed patches of the fault. Although it is difficult to determine the rupture front due to data resolution, a slower rupture velocity near the large slip region is still evident. This complicated variation can be further investigated by considering a non-linear dynamic rupture process analysis.

Figure 12 shows the map view of the slip distribution for the Chi-Chi earthquake. It is noteworthy that the largest slip region was in fact located at the turning portion of the Chelungpu

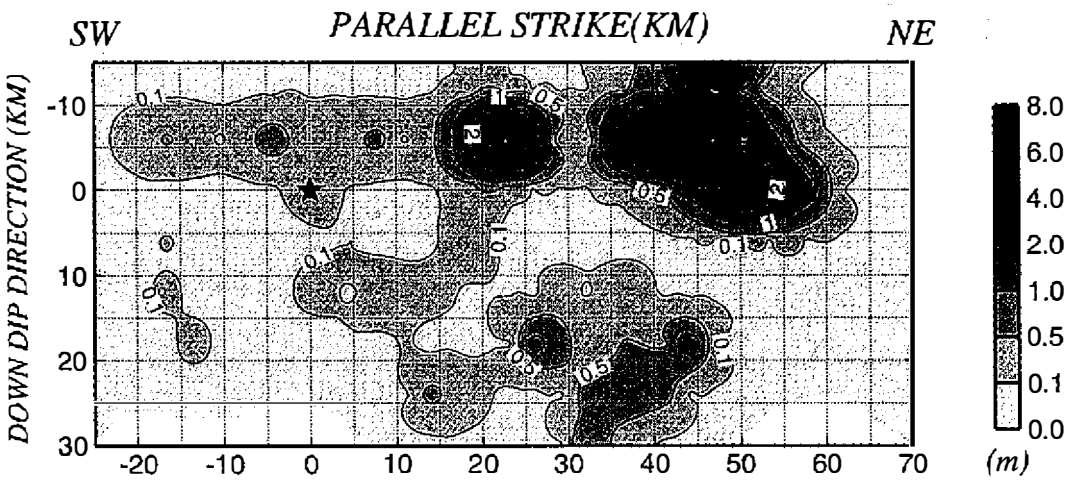

Fig. 9. Slip distribution of the multiple-time window model. The focal mechanism used in this model was strike =3°, dip=29°, rake=66°.

fault, and it was near the epicenter of the 1935 Hsinchu-Taichung earthquake (M_L=7.1). Also shown in Fig. 12 is the location of the larger aftershocks (M_L > 4). Although the precise locations of the aftershocks may not be certain, they are reasonably well correlated with the slip distribution. The large slip region showed the absence of aftershock, while large aftershocks clustered near the edge of regions with concentrated slip.

In general, slip distributions derived in the different models show similar patterns. The results from multi-time window analysis are presented for comparison with the observed surface displacement along the Chelungpu fault in Fig. 13. The spatial-slip distribution has very good agreement with geological observations (Lee and Cheng 2000; Ma et al. 2000). A larger number of slips occurred at 10 ~ 20 km north of the fault. The largest surface break occurred at about 45 ~ 50 km north of the epicenter. The spatial-slip distributions obtained in this study also coincide well with the near-source strong motion waveforms (Chung and Shin 1999; Ma et al. 2000). Large static offset can be noted for the displacement waveforms near the determined large slip region. A smaller amount of static offset is found for the stations near the southern portion of the fault. The slip distributions at the southern and northern portions of the fault show different rupture behavior. Table 3 lists the related fault parameters of the models used in the analysis.

4. CONCLUSIONS

The analysis of the teleseismic waveform inversion through different models consistently reveals a large asperity in the northern portion of the fault. An anomalous large slip region centers about 40 to 50 km north of the hypocenter at the shallow depth. The largest amount of slip was about 6 ~ 10 m. The slip near the vicinity of the hypocenter had a relatively smaller

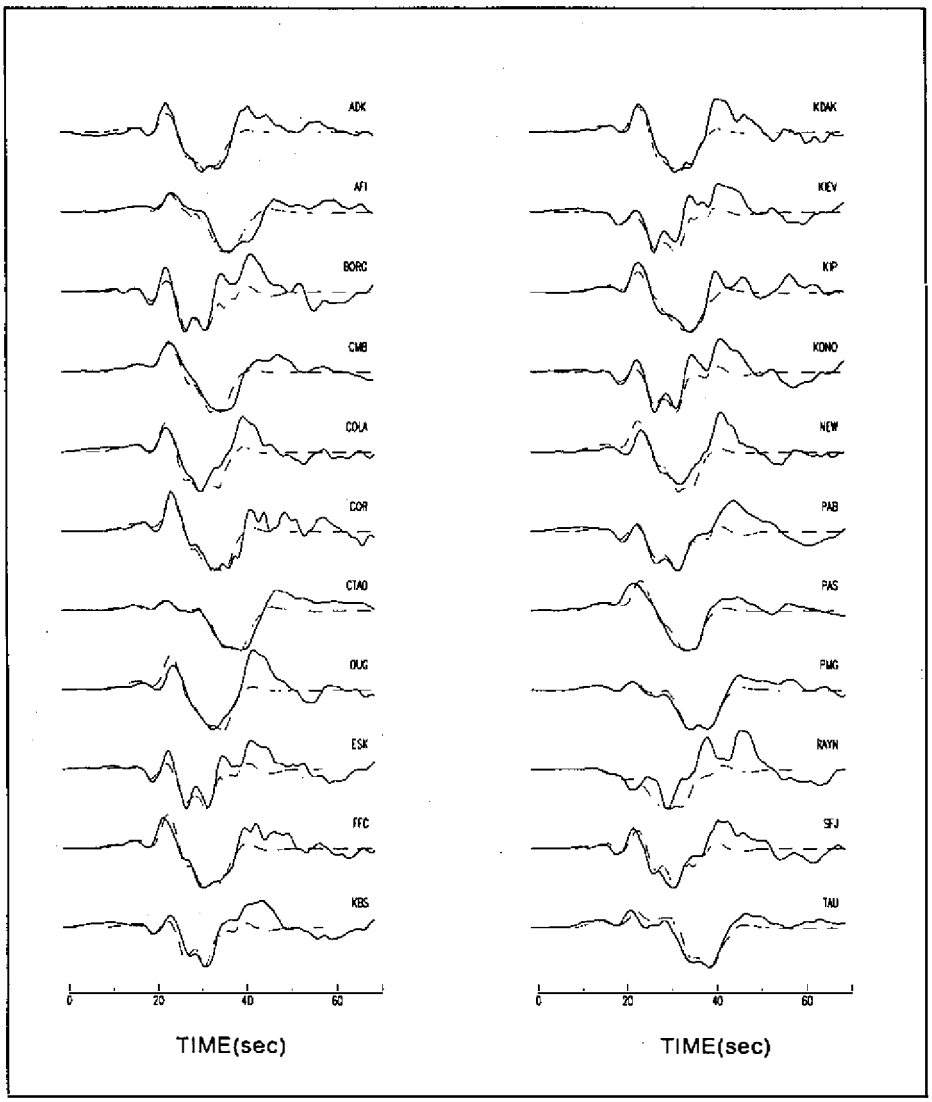

Fig. 10. Comparison of the observed (solid lines) and synthetic (dashed lines) waveforms for the multiple time window model of Figure 8.

amount of slip in these models. The spatial slip distribution pattern coincides well with the observed strong-motion displacement and surface break. In the largest dislocation region, the slip was dominated by dip-slip. Some strike-slip components in the middle of the fault were actually found during the rupture. The rupture velocity decelerated significantly within the asperity with large slips. The significant variations in slip amplitude, rake angle and rupture velocity in the models are quite comparable to those in the available geological data and near source strong motion waveforms.

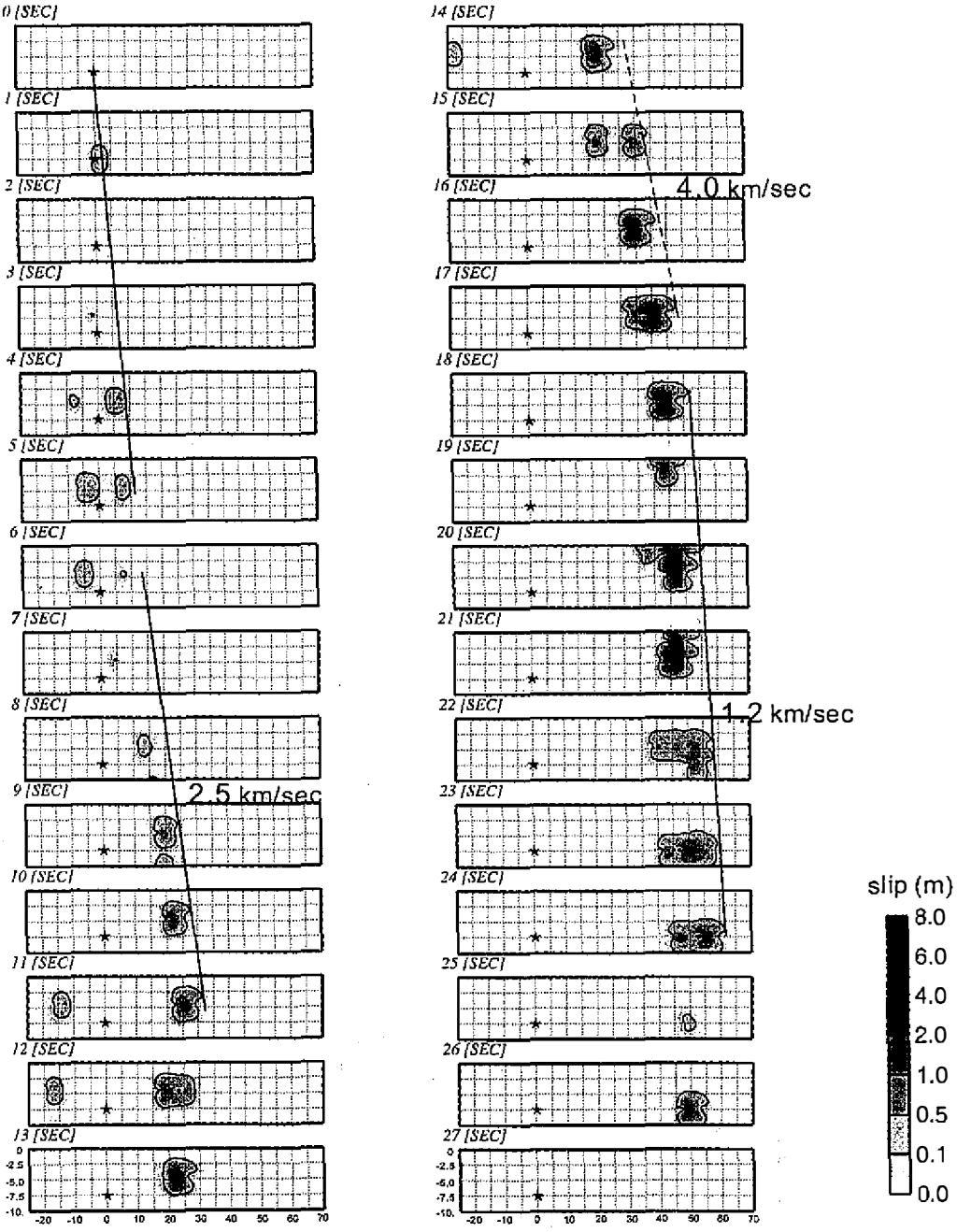

Fig. 11. Time progression of the Chi-Chi rupture for the multiple time window model given at intervals of 1 sec as labeled. The smallest contour is 0.1 m. The lines indicate selected regions of fairly constant rupture velocity. The dashed line indicates the roughly estimated rupture velocity.

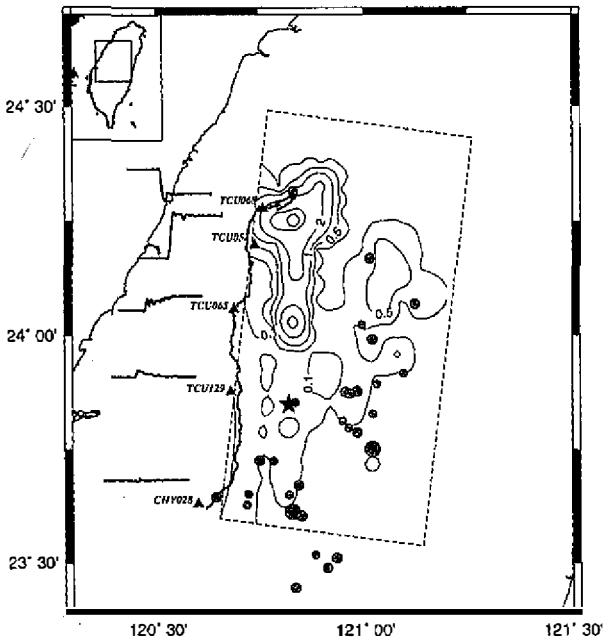

Fig. 12. Map view of the slip distribution. The epicenter is indicated with by a solid star. The small and large shaded circles indicate the aftershocks of magnitude 4 to 6. The solid triangles indicate the strong motion stations along the Chelungpu fault. The east-west displacement waveforms of the stations are also shown for reference.

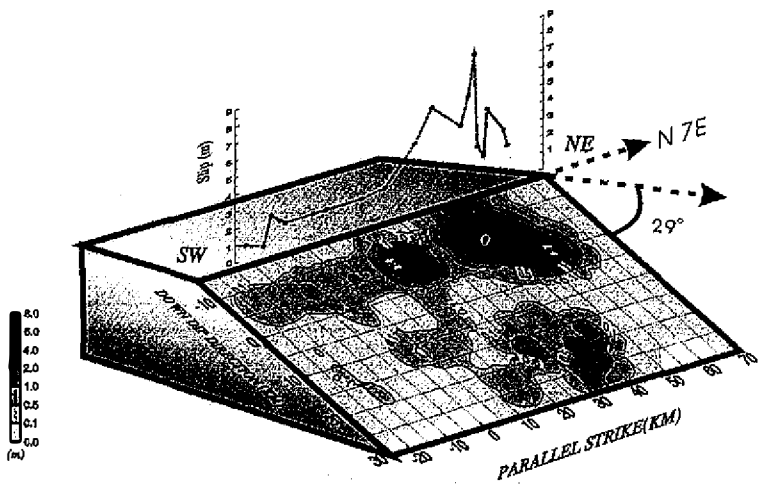

Fig. 13. Geometrical scheme of the slip distribution for comparison with the observed surface break (dashed line).

Table 3. Rupture model parameters.
*average slip in the asperity

Model	Mechanism (strike,dip,rake)	Moment ($*10^{27}$ dyne-cm)	Source time function (sec)	Average slip (m)*	Stress drop (bar)	M_w
Slip distribution	(3,29,66)	0.506	(1,0,1)	5	5.15	7.20
Strike-slip and Dip-slip distribution	(3,29,free from 0 to 90)	0.688	(1,0,1)	5	7.01	7.29
Temporal and Spatial slip distribution	(3,29,66)	0.500	Variable in 7sec	5	5.09	7.20

* average slip in the asperity

Acknowledgements We thank the suggestions from two anonymous reviewers. The discussions with Mr. T.R S. Song, Ms. H.-I. Wu and Prof. J. Mori had been very helpful. This work is under NSC89-2921-M-008-012-EAF.

REFERENCES

Archuleta, R., 1984: A faulting model for the 1979 Imperial Velley earthquake. *J. Geoph. Res.*, **89**, 4559-4585.

Chung, J. K., and T. C. Shin, 1999: Implications of the rupture process from the displacement distribution of strong ground motions recorded during the 21 September 1999 Chi-Chi, Taiwan earthquake. *TAO*, **10**, 777-786.

Hartzell, S. H., and T. H. Heaton, 1983: Inversion of strong ground motion and teleseismic waveform data for the fault rupture history of the 1979 Imperial Valley, California earthquake. *Bull. Seism. Soc. Am.*, **73**, 1553-1583.

Langston, C. A.. and D. V. Helmberger, 1975: A procedure for modeling shallow dislocation source. *Geophys. J.* **42**, 117-130.

Lee, C. T., and J. T. Cheng, 2000: Surface rupture of the September 20, 1999, Chi-Chi, Taiwan earthquake. (in preparation).

Liu, K.-S., T.-C. Shin, and Y. B. Tsai, 1999: A free-field strong motion network in Taiwan, TSMIP. *TAO*, **10**, 377-396.

Peyrat, S., R. Madariaga, and K. Olsen, 2000: Modeling earthquake source dynamics of the Landers 1992 eartqhuake, Taiwan-France Symposium on Nature Hazard Mitigation, 75-84.

Ma, K. F., C. T. Lee, Y. B. Tsai, T. C. Shin, and Jim Mori, 1999: The Chi-Chi, Taiwan Earthquake: Large surface displacements on inland thrust fault. *EOS*, **80**, 605-611.

Ma, K. F., T. R. Song, and Jim Mori, 2000: Dynamic rupture behavior of the 1999 Chi-Chi (M_W=7.7), Taiwan, Earthquake. Nature, submitted.

Ma, K. F., T. R. Song, S. J. Lee, and S. I. Wu, 2000: Spatial slip distribution of the September 20, 1999, Chi-Chi, Taiwan, Earthquake-inverted from teleseismic data. Geophys. Res. Let., revised.

Wald, D., and T. Heaton, 1994: Spatial and temporal distribution of slip for the 1992 Landers, California earthquake. *Bull. Seis. Soc. Am.*, **84**, 668-691.